Quantum Cascade Detectors

Fabrizio R. Giorgetta, Esther Baumann, Marcel Graf, Quankui Yang, Christian Manz, Klaus Köhler,
Harvey E. Beere, David A. Ritchie, Edmund Linfield, Alexander G. Davies, Yuriy Fedoryshyn,
Heinz Jäckel, *Member, IEEE*, Milan Fischer, Jérôme Faist, *Member, IEEE*, and Daniel Hofstetter

Abstract—**This paper gives an overview on the design, fabrication, and characterization of quantum cascade detectors. They are tailorable infrared photodetectors based on intersubband transitions in semiconductor quantum wells that do not require an external bias voltage due to their asymmetric conduction band profile. They thus profit from favorable noise behavior, reduced thermal load, and simpler readout circuits. This was demonstrated at wavelengths from the near infrared at 2 μm to THz radiation at 87 μm using different semiconductor material systems.**

Index Terms—**Intersubband photodetectors, quantum cascade detector, high-speed semiconductor photodetectors.**

I. INTRODUCTION

INTERSUBBAND (ISB) photodetectors, although first demonstrated already in 1987 in the form of photoconductive quantum-well infrared photodetectors (QWIPs) [1], remain a topic of high scientific and practical interest. Particularly at the energetic extremes of infrared radiation, namely in the low energy THz and in the high-energy near-infrared (NIR) ranges, there are still challenges in finding the best materials and designs for ISB photodetectors.

In the NIR, fast intraband semiconductor photodetectors are only available for wavelengths up to about 1.6 μm. On the other tail of optical frequencies, namely for detection of THz radiation, bolometers are widely used; however, they are not well suited for high-speed applications. For fast light detection at wavelengths above 1.6 μm, ISB photodetectors are very promising candidates. As unipolar devices, their fundamental speed limit is the ISB scattering time of electrons $\tau_{\text{scatter}} \approx 1$ ps. As an additional advantage, ISB detectors can be designed for a wide range of wavelengths in a single material system just by choosing adequate semiconductor layer thicknesses.

There are different working principles for ISB IR photodetectors; an overview is given, for example, by Schneider and Liu [2]. By far the most common design is the photoconductive (PC) QWIP, where the change of device resistance under illumination is determined by applying an external bias voltage across the detector and measuring the current at the same time. There are different types of PC QWIPs. In the widely used bound-to-quasi-bound QWIP, the detection energy is determined by the conduction band offset (CBO) between the quantum well (QW) and the barrier material. The active region consists of identical QWs separated by significantly thicker barriers to avoid coupling between the different QW states. The QW thickness and CBO (through the material composition) are chosen such that the second quantized electron level in the QW is close to resonance with the barrier's conduction band edge; this measure ensures a good carrier extraction efficiency under application of an appropriate bias voltage [3], but it also couples the detection wavelength to the CBO. By use of a bound-to-miniband design [4], the QWIP detection wavelength can be decoupled from the CBO. Today, QWIP focal plane array (FPA) cameras sensitive at wavelengths between 8 and 10 μm have reached commercial maturity and are used in military, security, surveillance, and medical applications. As an example, Gunapala *et al.* [5] presented a high-performance 1024 × 1024 pixel dual-band QWIP FPA based on GaAs–AlGaAs with cutoff wavelengths of 5.1 and 8.4 μm.

Compared with PC ISB photodetectors, the research on zero-bias photovoltaic (PV) ISB photodetectors has seen less progress. Schneider *et al.* [6], [7] observed pronounced photovoltaic effects in an asymmetric multi-QW (MQW) structure. The potential asymmetry was in this case introduced by a sheet of delta-doping close to the active QW. By use of another PV QWIP design, the so-called four-zone scheme [8], a 256 × 256 pixel FPA with a very low noise equivalent temperature difference of 5.2 mK in the 8–12-μm window was demonstrated [9]. According to Schneider [10], an optimized PV QWIP has superior noise properties, the capability to operate at higher photon fluxes, and an improved dynamical range in comparison to a PC QWIP. Hofstetter *et al.* [11] used a quantum cascade laser (QCL) structure as photovoltaic detector; this structure can be viewed as a prototype for the devices presented in this paper. Along these lines, a similar but optimized ISB detector was presented by Gendron *et al.* [12]; in analogy to the functioning of a QCL, this device was named quantum cascade detector (QCD). Just like the bound-to-miniband QWIP, QCDs

F. R. Giorgetta was with the University of Neuchatel, 2000 Neuchatel, Switzerland. He is now with the National Institute of Standards and Technology, Boulder, CO 80305 USA (e-mail: fabrizio.giorgetta@unine.ch).

E. Baumann is with the National Institute of Standards and Technology, Boulder, CO 80305 USA (e-mail: esther.baumann@unine.ch).

M. Graf is with the Department of Electrical and Computer Engineering, University of Waterloo, Waterloo ON N2L 3G1, Canada

Q. Yang, C. Manz, and K. Köhler are with the Fraunhofer Institute of Applied Solid State Physics, D-80001 Freiburg, Germany.

H. E. Beere and D. Ritchie are with Cavendish Laboratory, University of Cambridge, Cambridge, CB3 OHE, U.K.

E. Linfield and A. G. Davies are with the School of Electronic and Electrical Engineering, University of Leeds, Leeds, LS2 9JT, U.K.

Y. Fedoryshyn and H. Jäckel are with the Electronics Laboratory, ETH Zürich, CH-8092 Zürich, Switzerland.

M. Fischer and J. Faist are with the Institute of Quantum Electronics, ETH Zürich, CH-8093 Zürich, Switzerland.

D. Hofstetter is with the University of Neuchatel, 2000 Neuchatel, Switzerland (e-mail: daniel.hofstettser@unine.ch).
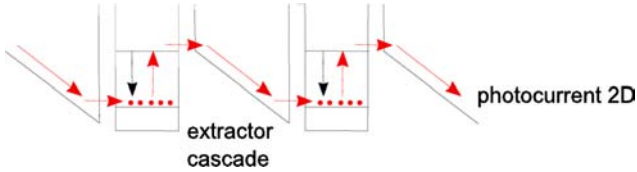
Fig. 1. Schematic conduction-band diagram of a QCD. By absorbing a photon, ground-level electrons are excited to the active QW's upper level. Due to the asymmetric band profile between two active QWs, the cascade excited electrons relax mostly in one direction (in this case to the right), resulting in a net photocurrent.
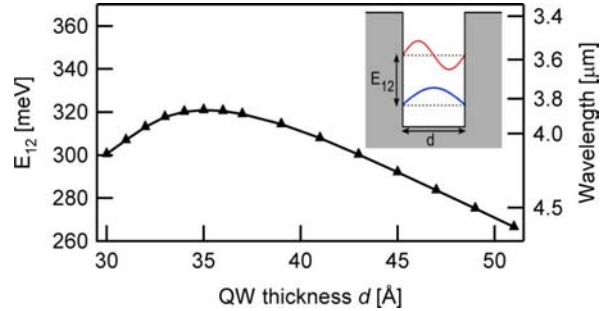

Fig. 2. Transition energy between the ground and the first excited state in an InGaAs–InAlAs QW lattice matched to InP as a function of QW thickness.

offer more design freedom for a given material composition. However, we will show below that a precise resonance condition must be fulfilled in these devices, just like in a PC QWIP. From this point of view, the epitaxial growth of such detectors is equally demanding as the one of a QCL or any other highly periodic device.

This paper discusses the theory and design principles of QCDs and presents the current state of research. The active region of a QCD is built up of multiple periods, each containing a thick, degenerately doped active QW and a nominally undoped extraction cascade composed of thinner QWs. The function of this cascade is to introduce an asymmetry in the conduction band potential such that photoexcited electrons have a preferential escape direction, resulting in a measurable net photocurrent. This is shown schematically in Fig. 1. As opposed to PC QWIPs, dark current is absent in PV QCDs. This leads to several advantages: no dark current noise occurs. The integration time in readout circuits can be extended, since the readout capacitance is not saturated by dark current. Finally, the thermal load of the detector is strongly reduced, which is of interest if the available cooling is limited, for example in space born systems or hand-held terrestrial staring systems. Although QCD devices have made substantial progress during the last few years [13], their potential advantage of a low Johnson noise is still limited by a too low device resistance, especially at room temperature. This problem must be overcome if QCDs are to stand their ground compared to QWIPs in terms of detectivity and operating temperature. Recent results presented in this paper show that QCDs with competitive performance can be achieved using improved designs based on better understanding of the limiting factors.

We will discuss the design principles of QCDs, as well as the choice of material system for the different detection wavelengths of the devices. Experimental results of QCDs at different wavelengths are reviewed and compared to alternative photodetectors at comparable detection wavelengths. First, QCDs based on InGaAs–InAlAs lattice matched to InP detecting between 5 and 17 μm are presented. As lattice-matched InGaAs QCDs can only detect wavelengths above ~4 μm due to the CBO of 520 meV, two alternative approaches are presented for shorter wavelengths: strained InGaAs–InAlAs and lattice-matched InGaAs–AlAsSb. A THz QCD detecting at 84 μm based on GaAs–Al$_{0.15}$Ga$_{0.85}$As is also discussed. Finally, a broadband QCD covering the wavelength region from 4.7 to 7.4 μm is shown.

II. THEORY AND DESIGN

A. QCD Detector Theory

The design process for QCDs is discussed with respect to the detection wavelength, the detectivity, and the responsivity. A more comprehensive theory on ISB transitions can be found, for example, in [14]. Conduction-band ISB devices such as QCDs are based on photon–electron interactions between quantized electron subbands in the conduction band of semiconductor heterostructures. Their spectral response is maximal at the energy separating two quantized electron levels in a QW. As opposed to semiconductor devices based on interband transitions, where the operating wavelength corresponds approximately to the bandgap and is given by the semiconductor material, the operating wavelength of ISB structures is thus mainly a function of the QW thickness. Fig. 2 shows the transition energy E_{12} between the two lowest electron levels in a QW as function of the QW thickness d obtained by numerically solving the Schrödinger equation for the QW. The reason for the nonmonotonous behavior of the curve towards thinner d is the upper QW level becoming resonant with the continuum. As soon as the upper level reaches the band edge of the barrier material, further decrease of the thickness d leads to a smaller transition energy.

The current responsivity R of a QCD is defined as detector output current I_S per unit of input signal power P_S and is given by

$$R = \frac{I_S}{P_S} = \frac{q}{h\upsilon}\eta g_p = \frac{\lambda q}{hc}\eta g_p \qquad g_p = \frac{p_e}{N_{\mathrm{QW}}p_c} \qquad (1)$$

where $\nu = c/\lambda$ is the signal frequency, λ is the signal wavelength, c is the vacuum speed of light, q is the elementary charge, h is Planck's constant, η is the absorption efficiency, and g_p is the photodetector gain; p_e is the escape probability of an excited electron in the active QW, p_c is its capture probability into the active QW's ground state for an electron traveling down the QCD's cascade, and N_{QW} is the number of active QW periods of the QCD. Optimization of R is thus accomplished through absorption efficiency and photodetector gain.

For a QCD, the absorption efficiency η is linked to the two-dimensional (2-D) absorption coefficient α_{2D} of the QCD's active (doped) QW by

$$\eta = 1 - e^{-N_{\text{QW}}\alpha_{2D}} \approx N_{\text{QW}}\alpha_{2D}, \quad \text{for } N_{\text{QW}}\alpha_{2D} \ll 1 \quad (2)$$

where α_{2D} is calculated using Fermi's golden rule

$$\alpha_{2D} = \frac{n_s q^2 \hbar}{2\varepsilon_0 c n m^*} f_{12} \frac{\Gamma}{(E_2 - E_1 - \hbar\omega)^2 + \Gamma^2}$$
$$f_{12} = \frac{2m^*\omega_{12}}{\hbar} |\langle\phi_1|z|\phi_2\rangle|^2 \quad (3)$$

where n_s is the active QW's 2-D doping (or sheet carrier) density, n is the refractive index of the QCD, and m^* is the effective electron mass in the QW, f_{12} is the oscillator strength between the two lowest wave functions in the active QW, ϕ_1 and ϕ_2, as a function of the position along the growth direction z, and Γ is the half-width at half-maximum (HWHM) of the intersubband transition's Lorentzian absorption shape. If $N_{\text{QW}}\,\alpha_{2D} \ll 1$, the absorption efficiency and the responsivity thus increase linearly with the number of periods and the doping density. However, since the detector gain is inversely proportional to the number of periods, the current responsivity is at least in first approximation independent from the number of periods.

Another common figure of merit for photodetectors is the detectivity $D^* = R_p/i_n\sqrt{A\Delta f}$, which is the ratio between peak responsivity R_p and mean noise current i_n normalized by the detector area A and the measurement bandwidth Δf. Its units are cm·Hz$^{0.5}$/W, also known as Jones. For a QCD and at temperatures above the so-called background limited infrared performance temperature T_{BLIP}, $i_n = i_n^J$ and $D^* = D_J^*$ are dominated by Johnson noise; at temperatures below T_{BLIP}, $i_n = i_n^{\text{BLIP}}$ and $D^* = D_{\text{BLIP}}^*$ are dominated by photon noise due to blackbody background radiation. Taking into account these different facts, we get for the detectivity of a QCD

$$D_J^* = R_p\sqrt{\frac{AR_0}{4k_BT}}$$
$$D_{\text{BLIP}}^* = \frac{R_p}{\sqrt{2q^2 g_p \int g_p \eta(\nu')\frac{d\Phi_{\text{BG}}(\nu')}{d\nu'}d\nu'}} \quad (4)$$

where R_0 is the differential device resistance around 0 V, T the device temperature, and $d\Phi_{\text{BG}}(\nu')/d\nu'$ the spectral background photon flux density.

Fig. 3(a) shows the schematic temperature dependence of a QCD's detectivity: below T_{BLIP}, the detectivity is background-limited ($D^* = D_{\text{BLIP}}^*$) and temperature-independent. At temperatures above T_{BLIP}, $D^* = D_J^*$ decreases with increasing temperature. D_{BLIP}^* is presented in Fig. 3(b) for an ideal ($\lambda < \lambda_c : \eta = 1, \eta = 0$ otherwise) photovoltaic detector as function of the cutoff wavelength λ_c for a 300 K background and a hemispheric field of view (FOV). For comparison, D_{BLIP}^* is shown also for a Lorentzian-shaped spectral sensitivity with a relative linewidth of 6%, which is a typical lineshape of a QCD. The Lorentzian shaped spectral sensitivity leads to an improvement of D_{BLIP}^* at detection wavelengths above 4 µm.
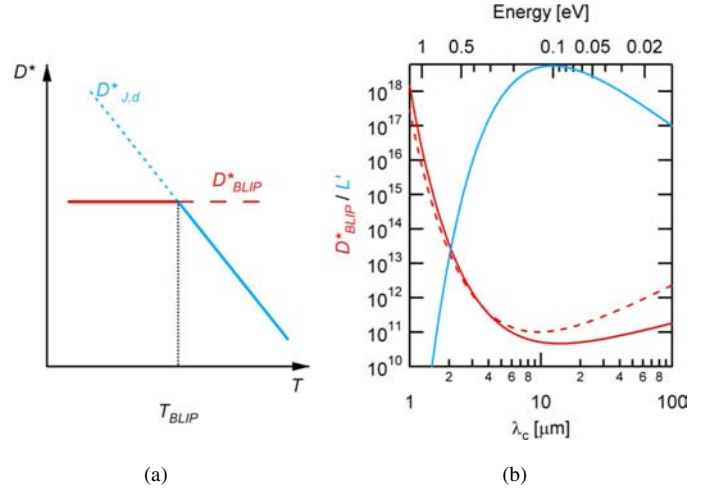

Fig. 3. (a) D^* as function of temperature. At T_{BLIP}, D_J^* crosses the background limited D_{BLIP}^*. (b) D_{BLIP}^* in Jones for a 300 K blackbody temperature, hemispherical field of view, and $\eta = 1$ (red) for an ideal photodetector (solid line) and a QCD with a Lorentzian spectral sensitivity peaking at λ_c with a fractional linewidth of 6% (dashed line); the blue line is the photon flux spectral density of a 300 K blackbody in [s^{-1}Hz^{-1}cm^{-2}sr^{-1}].
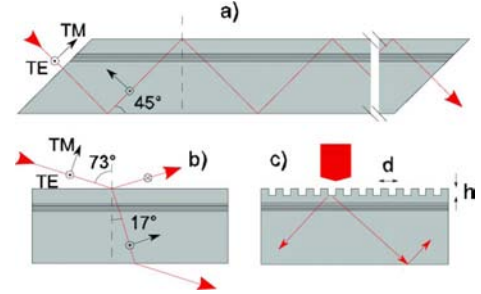

Fig. 4. Schemes of different ISB device geometries. (a) 45° multipass waveguide. (b) Brewster angle configuration (for InGaAs–InAlAs lattice matched to InP). (c) Grating coupler.

B. QCD Design

Sample Geometry: The quantum–mechanical polarization selection rule [15] states that only the electric field component perpendicular to the QW layers interacts with ISB transitions. The sample geometry of an ISB device must thus ensure that the internal light propagation is not perpendicular to the sample surface. Fig. 4 shows three common ISB detector geometries. The 45° wedge multipass geometry (a) has moderate processing requirements and allows for robust and reproducible sample characterization. It is thus often used to determine the performance of ISB photodetectors. Its biggest advantage is that there is no sensitivity on the detection wavelength. However, even when using TM polarized radiation, only 50% of the incoming light interacts with the ISB transition. The Brewster geometry (b) requires the least sample preparation, but has low conversion efficiency. It can thus be used for heavily absorbing samples only. A grating (c) has potentially the highest conversion efficiency and allows for 2-D detector arrays, but involves more sophisticated sample preparation. It is the usual geometry for industrial packaging.

Band Structure: The crucial design aspect of ISB devices such as QCDs is the quantum–mechanical bandstructure. It can
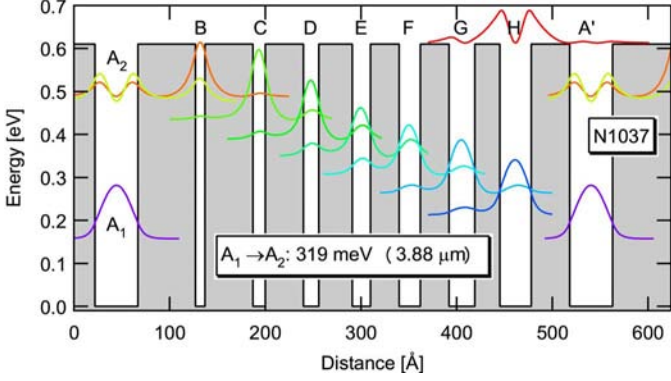
Fig. 5. Calculated conduction-band profile of QCD N1037. QW A is the active QW; QWs B–H form the extractor cascade.

be calculated using numerical solvers of the Schrödinger equation. A typical band structure of a QCD is shown in Fig. 5. QW A is the active QW which is degenerately doped (i.e., the Fermi level lies in the conduction band above the ground state A_1). QWs B-H form the electron extraction cascade and are nominally undoped. The transport from the active QW into the cascade is ensured through resonant tunneling between A_2 and the ground state of QW B; this allows for a thick barrier between the active QW and the extractor. By this feature, the interaction between active QW and intermediate extractor levels is reduced, which increases the device resistance without lowering the escape probability. To achieve an efficient electron extraction through phonon assisted scattering, the energy difference between the individual extractor states should be close to the longitudinal optical phonon energy E_{LO} (GaAs: $E_{LO} = 36$ meV, $In_{0.53}Ga_{0.47}As$: $E_{LO} = 32$ meV). As will be shown below, this design feature can be dropped if there is no requirement for high-speed operation.

Besides determining the QCD's detection energy and influencing the device resistance, the bandstructure has also an impact on the gain g_p (1), which is proportional to p_e/p_c. For a QCD, the capture probability p_c is close to unity. The escape probability p_e can be approximated by the phonon scattering lifetimes from the upper resonant state A_2 or B_1 towards the ground state A_1 (relaxation time, τ_{rel}) and towards the extractor state C_1 (escape time, τ_{esc})

$$p_e \approx \frac{\tau_{rel}}{\tau_{rel} + \tau_{esc}} \tag{5}$$

where τ_{rel} and τ_{esc} are calculated using the electron wavefunctions from the simulated conduction band diagram. A high gain can thus be obtained by designing the bandstructure in a way that $\tau_{rel} \gg \tau_{esc}$.

Koeniguer *et al.* [16] presented a model based on a standard electron–optical phonon Hamiltonian which calculates the intersubband diffusion and thus the resistance of QCDs. Although the basic assumptions of this model are very reasonable, we usually only achieved qualitative agreement with our experimental data. In addition, the validity of the model could be verified in selected temperature ranges only.
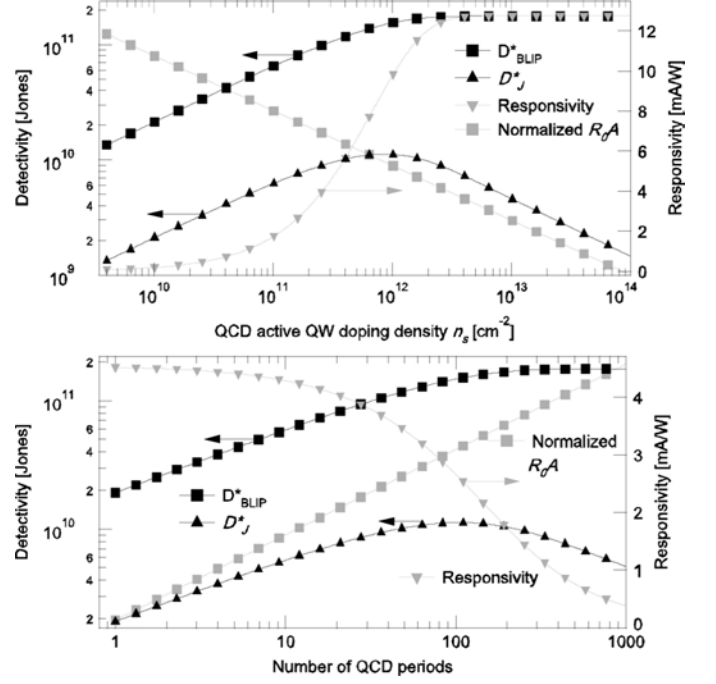

Fig. 6. QCD detectivity, responsivity, and resistance area product R_0A for varying doping density and number of periods. The vertical scaling of the normalized R_0A is logarithmic. The calculations are based on the values of QCD N1021 at a temperature of 100 K; it has 30 periods and a sheet carrier doping density of 2.46×10^{11} cm^{-2} in the active QW.

Doping and Number of Periods: For a QCD, the detectivity D^* is maximized by ensuring a high device resistance (thus a low Johnson noise) without lowering the escape probability and thus the efficiency. The most important design parameters are the layer thicknesses (determining the band profile as discussed above), the doping density n_s of the active QW, and the number of periods N_{QW}.

As long as the absorbance $N_{QW} \alpha_{2D} \ll 1$, so that $\eta \approx N_{QW}\alpha_{2D}$, the absorption η and thus the responsivity R are proportional to the doping density n_s [see (3) and (1)]. It follows from (4) that D^*_{BLIP} is proportional to $\sqrt{n_s}$. As the device conductance is linear in n_s, this is also true for D^*_J. This does, however, not imply that n_s should be as high as possible. η cannot become larger than 1 and therefore saturates for high doping concentrations. In the example shown on the top panel of Fig. 6, this starts to be the case at $n_s \approx 2 \times 10^{11}$ cm^{-2}. Therefore, R and D^*_{BLIP} also saturate, whereas $D^*_J \propto 1/\sqrt{n_S}$ decreases with a further increase of n_s. Assuming again that $N_{QW}\alpha_{2D} \ll 1$ and thus $\eta \propto N_{QW}$, R is independent from the number of periods N_{QW} and D^*_{BLIP} increases with $\sqrt{N_{QW}}$. As the device resistance grows linearly with N_{QW}, the same is true for $D^*_J \propto \sqrt{N_{QW}}$. For large N_{QW}, the aforementioned assumption is not true anymore, η and D^*_{BLIP} saturate, R is proportional to $1/N_{QW}$, and D^*_J is proportional to $1/\sqrt{N_{QW}}$. The calculated dependencies of D^*_J, D^*_{BLIP}, and R on N_{QW} for a typical QCD, namely N1020 (parameters will be given below), are shown on the bottom panel of Fig. 6. As a conclusion, we notice that, for any doping density, an ideal number of periods must be found.

TABLE I
MIR QCDs

	N538	N1020	N1021	N1022	N973
E_{12}	230	118	165	266	71.3
	(5.4)	(10.5)	(7.5)	(4.7)	(17.4)
n_{cnt}	16	6	10	20	3
n_{QW}	4	2	3	4	1
A	59 / 60	107 / 50	82 / 60	51 / 75	153 / 55
B	17 / 44	40.5 / 47	28 / 57	34 / 55	63 / 40
C	20 / 39	48 / 45	34 / 55	14.5 / 64	66 / 36
D	23 / 37	62 / 41	42 / 51	55 / 58	70 / 32
E	27 / 35	-	55 / 58	20 / 77	73 / 30
F	32 / 31	-	-	24 / 75	74 / 24
G	39 / 28	-	-	29 / 71	-
H	47 / 26	-	-	35 / 68	-

Growth parameters of the MIR QCDs along with the simulated detection energy E_{12} in meV and the corresponding wavelength in (µm), and the Si doping densities n_{cnt} (upper and lower contact layer) and n_{QW} (QW A) in 10^{17} cm^{-3}. The layer thicknesses are given in Å for one period in QW / barrier pairs which are alphabetically labeled in a similar way as shown in the band diagram in Fig. 5.

III. QCD Devices

Here, experimental results of QCD devices are presented. All samples were grown by molecular beam epitaxy (MBE) in order to achieve a high interface quality between QWs and barriers. The samples were polished into 45° multipass waveguides; for photocurrent measurements, mesas were processed on top of one of the 45° facets using standard photolithography and wet etching. Contacting was obtained through evaporated metal contacts.

A. Mid-Infrared QCD

For this study, mid-infrared (MIR) is considered as radiation encompassing wavelengths from 5 to 30 µm. There are various photodetector applications in this spectral range. Heat seeking of hot targets such as aircraft engine exhaust plumes takes place between 3 and 8 µm. Sensitive ISB detectors with a narrow linewidth can be an interesting choice to determine the amount of certain molecules or atoms in gases and liquids by measuring their characteristic absorption lines. Another potential application for fast MIR photodetectors is heterodyne spectroscopy, which allows distinguishing spectrally close absorption lines as the potentially high resolution of this method requires an electrical detector bandwidth in the GHz range. Thermal imaging in the MIR is of general interest as the emission of a room temperature black body peaks at 10 µm. Cameras detecting around 10 µm with a low-noise equivalent temperature difference are thus commonly used in construction to detect thermal bridges, in fire protection to pinpoint pockets of embers, in various security and military applications such as missile detection, as well as in medical spectroscopy. Here, the experimental results obtained from QCDs sensitive at wavelengths between 4.7 and 17 µm (71–260 meV) are presented. All investigated samples consist of In$_{0.52}$Ga$_{0.48}$As QWs and In$_{0.53}$Al$_{0.47}$As barriers lattice matched to InP substrates.

In Table I, the active region layer thicknesses for samples N1020, N1021, and N1022 detecting at 10.5, 7.5, and 4.7 µm are listed. Growth started with a 6000-Å-thick In$_{0.53}$Ga$_{0.52}$As lower contact layer followed by 30 repetitions of the active
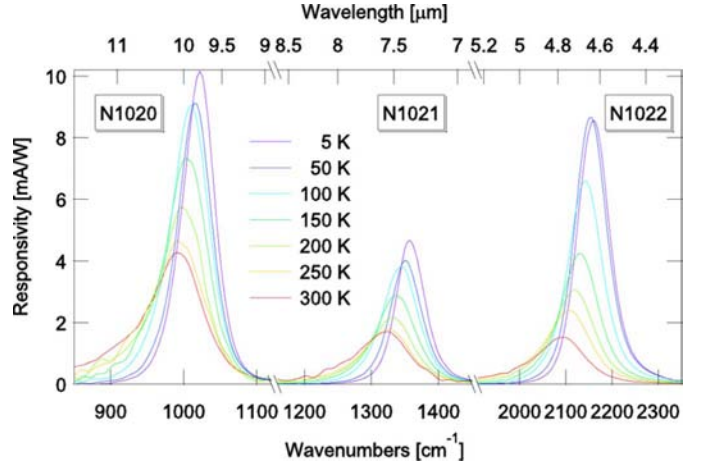

Fig. 7. Responsivity of the ISB $A_1 \rightarrow A_2$ transition of N1020 (left), N1021 (center), and N1022 (right) at different temperatures.

region and a 2000–Å-thick In$_{0.53}$Ga$_{0.47}$As upper contact layer. From a design point of view, those samples are based on the 5-µm QCD N538 [17], whose active layer is also described in Table I; however, they have thicker barriers to increase the device resistance. The active QW A is degenerately doped, whereas the other QWs (forming the extractor) are undoped. Fig. 7 shows the measured responsivity spectra of the three samples at different temperatures; all three devices worked up to room temperature. For N1022 and N1021, the peak detection energy at 5 K of 268 meV, respectively, 168 meV corresponds well to the simulated one of 266 and 165 meV; for N1020, the observed value of 127 meV is 8% above the designed 118 meV. Although not determined unambiguously, the origin of this blueshift lies most probably in a QW thickness deviation: for a 4% thinner QW, the simulated A1 → A2 ISB transition energy corresponds exactly to the measured value. The observed redshift of detection energy with increasing temperature (N1020: 127 meV at 5 K, 123 meV at 300 K) is typical for QCDs and caused by band filling and nonparabolicity of the electron states [18].

Fig. 8 shows the Johnson noise-limited detectivity for all three samples as a function of temperature obtained with (4) using measured values for the responsivity and $R_0 A$; the constant background limited detectivities are also shown. The detectivity of N1022 becomes background limited at $T_{BLIP} = 45$ K, whereas N1020 does not reach the BLIP condition.

Fig. 9 shows the calculated conduction band diagram of sample N973 designed for a detection energy (corresponding to the $A_1 \rightarrow A_2$ transition) of 71.3 meV (17.4 µm) [19]; its active region is described in Table I as well. Given the low detection energy and the In$_{0.53}$Ga$_{0.47}$As LO phonon energy of 32 meV, the phonon stair QCD extractor would have only two steps. Such a single QW extractor would result in strong coupling between adjacent active QW ground states and thus a low device resistance and a high Johnson current noise. To reduce this undesired ground state coupling, the center rung of the phonon stair is replaced by a chirped miniband formed by several QWs and barriers with similar thicknesses. Thus, a photoexcited
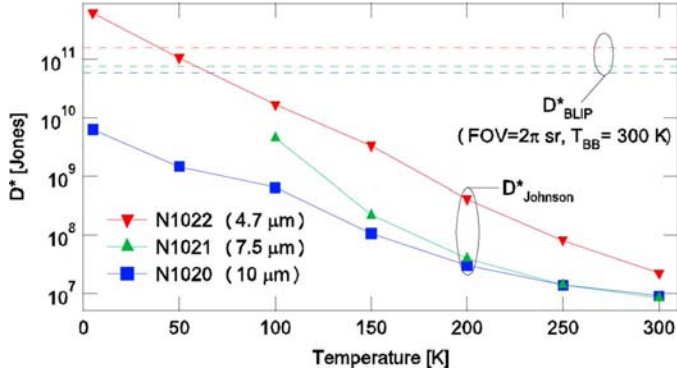
Fig. 8. Detectivities D^* of N1020, N1021, and N1022 as function of temperature. D^* is Johnson noise-limited except for N1022 below $T_{\mathrm{BLIP}} = 45$ K. The dashed lines on top represent the background limited detectivity D^*_{BLIP} for a hemispherical FOV and a background temperature of 300 K.
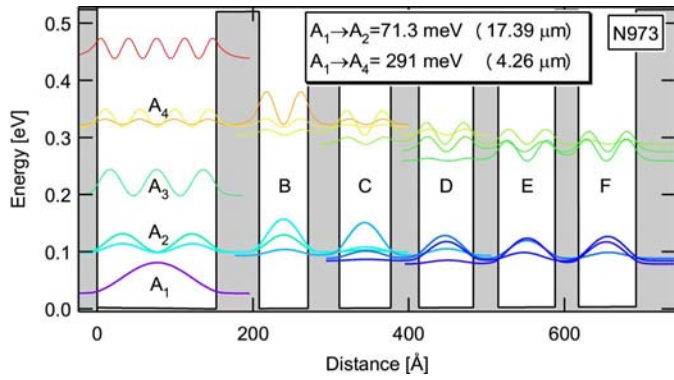

Fig. 9. Calculated conduction band profile of the 17 μm QCD N973. Photoexcited electrons can tunnel from A_2 through the C_1-F_1 miniband to the next period.
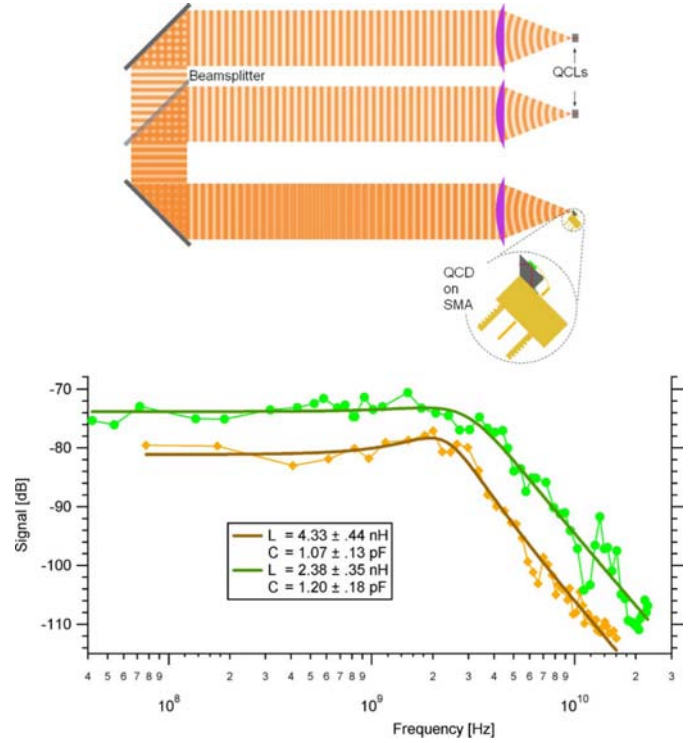

Fig. 10. Top: Schematic of heterodyne setup using the beat between two QCLs with slightly different emission wavelengths around 5.46 μm to measure the QCD's frequency response. Bottom: frequency responses of the 5.3 μm QCD N538 operated at room temperature. Green circles correspond to a device with a 2.5-mm-long bond wire, whereas the brown diamonds correspond to a 4.5-mm-long bond wire. The solid lines are fits using a *RLC* QCD model.

electron in level A_2 tunnels to the B_1-F_1 miniband and, due to this miniband's asymmetry, is collected into the ground state of the next period. This is a typical case where the design rule of one LO-phonon energy between adjacent extractor states has been dropped.

At 5 K, the responsivity of N973 peaks at 75.0 meV with 11 mA/W. Based on the measured responsivity and device resistance, a Johnson noise limited detectivity $D^*_J = 10^{11}$ Jones at 5 K was calculated using (4). The photon noise limited BLIP detectivity for a 300 K background and a hemispheric FOV is 1.22×10^{11} Jones, wherefore T_{BLIP} is below the investigated temperature range for N973.

To estimate the gain of N973, the absorption was calculated with Fermi's golden rule (3) using the full-width at half-maximum (FWHM) extracted from the responsivity measurements. For a double pass through the active region, the calculated absorption efficiency amounts to 38%; inserting this value together with the measured peak responsivity into (1) results in an escape probability p_e of 6%. This low value is probably caused by the high barriers resulting in a low A_2-B_1 miniband width and thus a low tolerance for the layer thicknesses: a small deviation from the nominal value breaks up the A_2-B_1 miniband resulting in a greatly reduced extraction efficiency.

High-frequency testing: The frequency response of the 5.46 μm QCD, N538, was tested using a heterodyne beat setup [20].

For this experiment, the detector was glued directly on an SMA connector, connected to its central conductor with a short bond wire, and tested at room temperature only. As schematically shown in Fig. 10, the optical input signal was generated by two collinearly overlaid CW operated DFB QCLs with identical emission wavelengths around 5.4 μm. By modifying the drive current of one of the QCLs, its emission frequency is shifted resulting in a beat signal with a repetition rate equal to the difference frequency between both QCLs. Fig. 10 shows the response of N538 to the beat measured with a spectrum analyzer for two different bond wire lengths. The signal has a second order low-pass characteristic which can be described with an electrical resistance–inductance–capacitance (*RLC*) circuit taking into account the parasitic capacitance of the QCD and the bond wire inductance. With the shorter bond wire, the cutoff frequency of N538 is 4 GHz and a signal was observed up to 23 GHz. The excellent agreement between the simple theoretical description and the experiment confirms that the frequency response is clearly limited by the sample mount; a theoretical estimation of N538's intrinsic frequency limit based on phonon-electron scattering times results in a cutoff frequency of roughly 65 GHz. This is in good agreement with heterodyne QWIP measurements, where signals at frequencies up to 82 GHz were observed [21].

The measured characteristics of the MIR QCDs correspond generally very well to the nominal values, which proves the maturity of the $In_{0.53}Ga_{0.47}As$–$In_{0.52}Al_{0.48}As$ material system as well as the robustness of the QCD design. Compared to

commercial liquid nitrogen cooled mercury–cadmium–telluride (MCT) detectors and GaAs–AlGaAs QWIPs, the D^* of QCDs is lower: At 5 μm, MCTs have a $D^* = 1 \times 10^{11}$ Jones compared with 0.6×10^{11} for N1022 at 75 K. At 10 μm, MCTs reach $D^* = 5 \times 10^{10}$ Jones, whereas N1020 reaches 0.1×10^{10} Jones at 75 K. To improve MIR QCDs, the escape probability, absorption efficiency, and device resistance should be further increased. To obtain a higher resistance and absorption efficiency, the barrier thicknesses at the low energy end of the extractor needs to be enlarged. By increasing the optical overlap between the highest extractor state and the excited state of the active QW and, additionally, the overlap between the highest and the second highest extractor states, the escape probability can be improved. Also, the commercial potential in QCDs lies not necessarily in superior D^* but in high-speed photovoltaic operation in the infrared together with low-cost production by using well-established semiconductor materials.

B. Near-Infrared QCDs

An industrially significant field for near infrared (NIR) photodetectors are long-haul fiber communications, which depend on fast optoelectronic devices sensitive at 1.5 μm as the glass fiber attenuation is minimal at this wavelength. The second atmospheric window between 3 and 5 μm is interesting for eye-safe free-space optical communication links, but also for high-precision time-of-flight measurements used in 3-D imaging. To realize ISB photodetectors in the NIR, the semiconductor heterostructures presented in the previous MIR section are not appropriate: for $In_{0.53}Ga_{0.47}As$–$In_{0.52}Al_{0.48}As$ material with a CBO of 520 meV, the highest ISB energy between ground state and first excited state is around 320 meV for a QW thickness of 34 Å. For the GaAs–$Al_xGa_{1-x}As$ system with a CBO of up to 1 eV, the maximal E_{12} is 550 meV for a 22-Å QW with $x = 1$ and $E_{12} = 220$ meV for a 39-Å QW with $x = 0.39$ (for $x > 0.39$, the bandgap of $Al_xGa_{1-x}As$ becomes indirect). To reach higher ISB transition energies, a material combination with a larger CBO is required. There exist several alternative semiconductor heterostructures with large CBOs, each of whom has its own advantages and drawbacks: strain compensated $In_{x>0.53}Ga_{1-x}As$–$In_{x<0.52}Al_{1-x}As$ builds upon the mature lattice matched $In_{0.53}Ga_{0.47}As$–$In_{0.52}Al_{0.48}As$ system, but for a significant enhancement of the CBO, the large introduced strain severely hampers the growth. $In_{0.53}Ga_{0.47}As$–$AlAs_{0.56}Sb_{0.44}$ is lattice matched to InP and has a CBO of 1.6 eV; however, growth of AlAsSb is less mature, the abruptness of its interface towards InGaAs is reduced by interdiffusion, and the conduction band minimum of AlAsSb is 789 meV lower in the X valley compared with the Γ valley [22]. InAs–AlSb has a CBO of 2.1 eV, but suffers from strain. Group III nitrides (AlN, GaN, InN and their alloys) offer a large range of CBOs, for example, 1.9 eV for AlN–GaN, and have a direct band gap, but their large lattice mismatches and the lack of lattice-matched substrates with low defect densities makes growth difficult. Nevertheless, nitride-based intersubband detectors at telecommunication wavelengths have been successfully demonstrated [23], [24]. As for QCDs, NIR devices based on strain compensated InGaAs–InAlAs and on $In_{0.53}Ga_{0.47}As$–$AlAs_{0.56}Sb_{0.44}$ were demonstrated.

TABLE II
NIR QCDs

	N1037	3392	EP745	3394
E_{12}	319 (3.89)	572 (2.17)	572 (2.17)	761 (1.63)
n_{cnt}	1	8	1	8
n_{QW}	1	2	2	2
A	45 / 60	30 / 26	30 / 24	23.4 / 30
B	10 / 50	11 / 19	11 / 19	7 / 25
C	13 / 40	13 / 18	13 / 18	8 / 22
D	16 / 35	15 / 17	15 / 17	9 / 21
E	19 / 30	17 / 16	17 / 16	10 / 20
F	22 / 30	19 / 15	19 / 16	12 / 19
G	27 / 26	22 / 14	22 / 17	14 / 17
H	33 / 40	26 / 13	26 / 23	16 / 16
J	-	-	-	18 / 15
K	-	-	-	20 / 13

Growth parameters along with the simulated detection energy E_{12} in meV and the corresponding wavelength in (μm), and the Si doping densities n_{cnt} (upper and lower contact layer) and n_{QW} (QW A) in 10^{18} cm^{-3}. The layer thicknesses are given in Å for one period in QW / barrier pairs which are alphabetically labeled in a similar way as shown in the band diagram in Fig. 5 and Fig. 12.

Strained InGaAs–InAlAs: The CBO of $In_xGa_{1-x}As$–$In_yAl_{1-y}As$ heterostructures can be heightened from the lattice-matched value of 0.52 eV at $x = 0.53, y = 0.52$ by increasing the In content above 53% in the InGaAs QW and reducing it below 52% in the InAlAs barrier. However, the modified In contents introduce strain between the barrier and QW layers and the InP substrate; since the strains are of opposite signs, namely tensile in the barrier and compressive in the QW, a strain compensated pseudomorphic active region can be obtained by choosing appropriate layer thicknesses and material compositions. Using strained $In_{0.61}Ga_{0.39}As$–$In_{0.42}Al_{0.55}As$ with a CBO of 610 meV [25], a QCD (N1037) with a peak detection energy of 319 meV (3.88 μm) is presented [26]. N1037's active region is described in Table II. It consists of 60% barrier material; hence there is a small residual strain of 0.1% towards the InP substrate. Due to the relatively thin total thickness of the detector, this small lattice mismatch did not lead to a relaxation of the crystal.

The measured responsivity shown in Fig. 11 amounts to 8.9 mA/W at 318 meV (3.9 μm) and at 5 K. The measured transition energy corresponds well to the simulated $A_1 \rightarrow A_2$ ISB transition energy of 319 meV, demonstrating that both growth and simulation of 0.5% strained InGaAs–InAlAs heterostructures have a high maturity comparable to lattice-matched InGaAs–InAlAs. The spectral lineshape of the 300 K responsivity is identical to the one of the measured room temperature absorption also shown in Fig. 11. N1037's relative responsivity linewidth increases from 14 meV (4.4%) at 5 K to 21 meV (6.6%) at 300 K. The linewidth broadening comes along with a peak absorption energy redshift of -0.275 cm^{-1}/K displayed in the inset of Fig. 11. Both broadening and redshift are again due to band filling and nonparabolicity. Inserting the measured room temperature peak absorption per double pass of 6% and the corresponding peak responsivity of 5.8 mA/W into (1) results in a 30% escape probability p_e of photoexcited electrons from A_2 into the extractor. This is 2–3 times higher compared
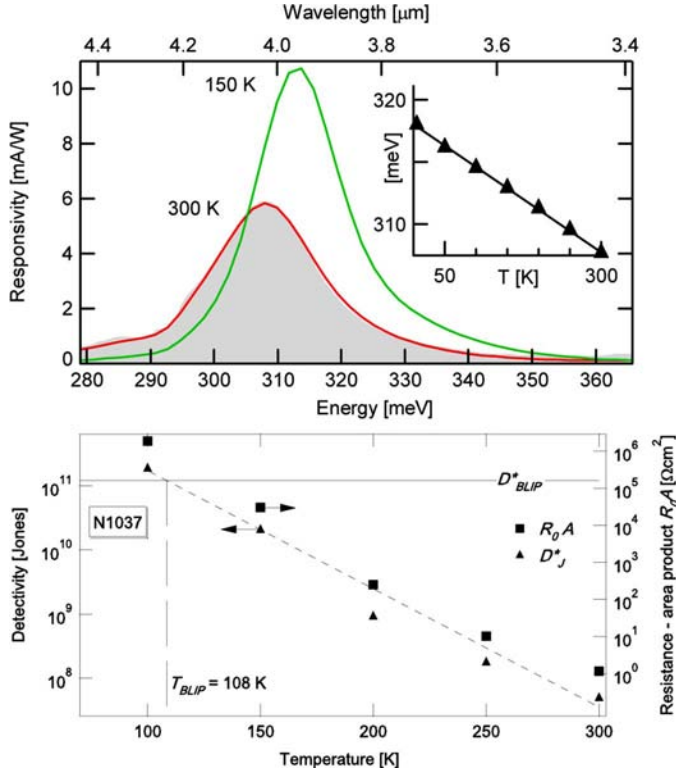
Fig. 11. Strained InGaAs QCD N1037. Top: responsivity spectra at 150 K and 300 K, along with the absorption lineshape measured at 300 K. Inset: peak responsivity energy extracted from a Lorentzian fit as function of temperature. Bottom: Johnson noise-limited detectivity D_J^* and resistance area product around 0 V $R_0 A$ for different temperatures. D_J^* equals the background-limited detectivity D_{BLIP}^* (FOV: 2π sr, 300 K background) at $T_{BLIP} = 108$ K.
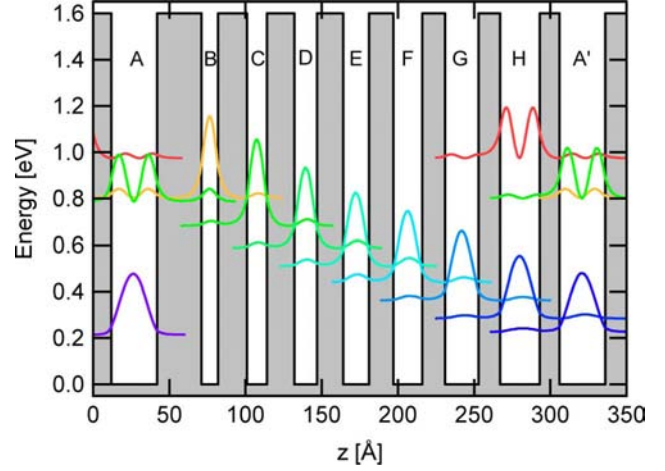

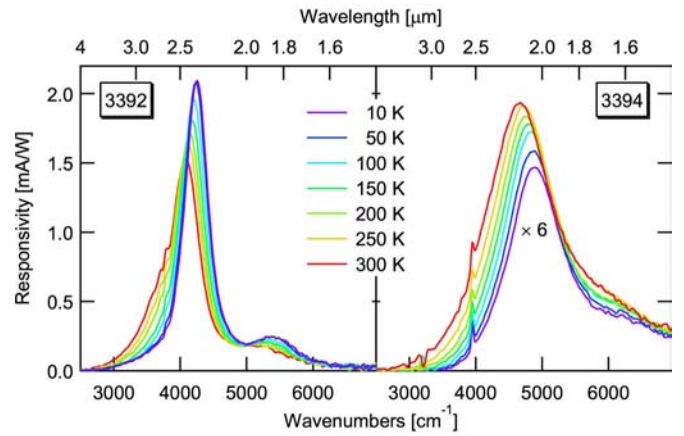Fig. 12. Calculated conduction-band profile of AlAsSb QCD 3392. QW A is the active QW; QWs B-H form the extractor cascade.

Fig. 13. Responsivity spectra of InGaAs–AlAsSb QCDs for different temperatures. Left panel: 3392 detecting around 4065 cm^{-1} (2.45 μm). The shoulder at 1.82 μm is due to the diagonal transition from the active QW's ground state A_1 into the last extractor QW's excited state H_2. Right panel: responsivity of 3394 detecting around 2.05 μm scaled by a factor of 6.

with the lattice-matched $In_{0.53}Ga_{0.47}As$–$In_{0.52}Al_{0.48}As$ QCDs presented in the previous section. This behavior is consistent with N1037's higher tunneling transition probability T_e from the state A_2 and B_1 calculated using [27]

$$T_e = \exp\left(-\sqrt{\frac{8m^*m_0\Delta E q}{\hbar^2}}t_b\right) \qquad (6)$$

where ΔE is the remaining barrier height and t_b the barrier thickness. For the 4.7-μm QCD N1022, $p_e = 12.5\%$ and $T_e = 1.3\%$, whereas for N1037, $p_e = 30\%$ and $T_e = 3.3\%$.

The Johnson noise-limited detectivity D_J^* of N1037 was calculated with the measured $R_0 A$ and peak responsivities; it equals 4.9×10^7 Jones at 300 K and reaches the background-limited detectivity $D_{BLIP}^* = 1.2 \times 10^{11}$ Jones (for 300 K background temperature and a hemispherical FOV) at $T_{BLIP} = 108$ K. This improvement over the longer wavelength QCDs presented in the MIR section, where only N1022 with a detection wavelength of 4.7 μm reached the BLIP condition at $T_{BLIP} = 45$ K is expected: at shorter wavelengths, the higher electron states and thicker barriers of a QCD result in an increased resistance R and thus a lower Johnson noise current $i_n \propto \sqrt{R}$ and a higher $D^* \propto 1/i_n$.

Antimony-based QCDs: To obtain ISB detectors working at wavelengths below 3 μm, the QCD design was also successfully applied to the $In_{0.53}Ga_{0.44}As$–$AlAs_{0.56}Sb_{0.44}$ material system lattice-matched to InP substrates, which offers a CBO of 1.6

eV. Other advantages besides the high CBO are that the mature processing technology of the InGaAs–InAlAs system can be used, that growth of the InGaAs QWs is well established, and that high-quality InP substrates are available at low cost. The difficulties lie in the growth of the $AlAs_{0.56}Sb_{0.44}$ barrier material and the barrier/QW interface quality. In real devices, the resulting interface fluctuation between QWs and barriers is a limiting factor towards high ISB transition energies [28]. Also, in a thin $In_{0.53}Ga_{0.44}As$ QW the upper level, A_2, lies above the lowest X-valley point for ISB transition energies A_2–$A_1 \geq 335$ meV (3.7 μm) [29], wherefore $\Gamma - X$ inter-valley scattering is expected to degrade the extraction efficiency and thus the overall performance of short wavelength InGaAs QCDs. Fortunately, $\Gamma - X$ inter-valley scattering was recently shown to be much slower in thin InGaAs–AlAsSb QWs as compared with bulk InGaAs [30].

In Fig. 13, the responsivity spectra of samples 3392 and 3394 are depicted [31]; growth parameters are listed in Table II and the calculated bandstructure is shown in Fig. 12. The responsivity peaks at 605 meV (2.05 μm) for 3394 and at
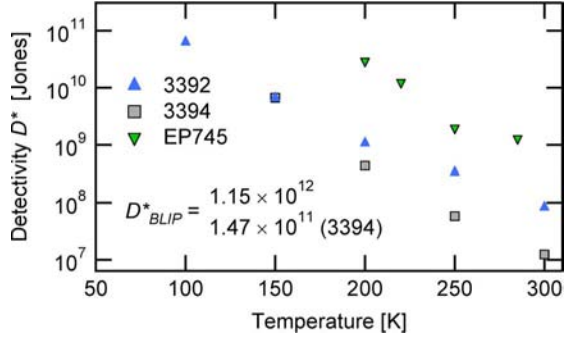
Fig. 14. Measured detectivities of the InGaAs/AlAsSb QCDs. The T_{Blip} values presented in the text are obtained by linearly (on the semilog scale) extrapolating the measured D^* values towards lower temperatures until they cross the temperature independent D^*_{BLIP} at the temperature T_{BLIP}.
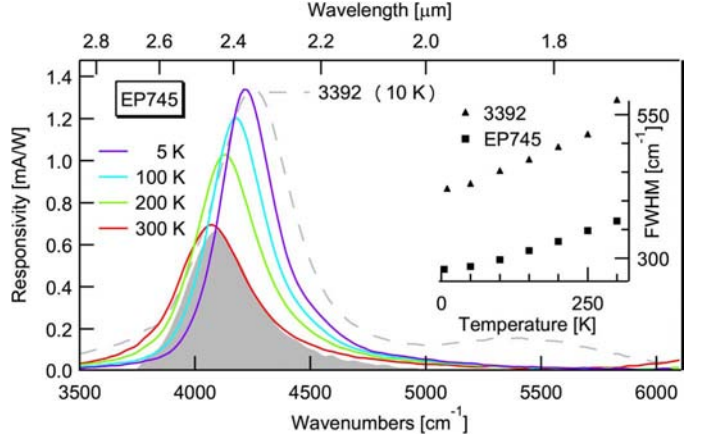

Fig. 15. Responsivity of InGaAs–AlAsSb QCD EP745 at different temperatures (solid lines). The dashed line is the responsivity of 3392 at 10 K scaled by a factor 0.64. The shaded area is the room temperature absorption per double pass of EP745 with a peak value of 3.4%. The inset compares the FWHM of EP745 to 3392.

528 meV/2.35 μm for 3392. Compared with the simulated E_{12} ISB transition energies, the measured values are lower by 8% (3392), respectively, 20% (3394). The increase of the deviation between measured and simulated ISB transition energy for decreasing QW thickness is consistent with the findings of Neogi *et al.* [32], who investigated ISB absorption spectra in InGaAs–AlAsSb QWs with varying thicknesses. They observed an ISB transition energy of 650 meV as opposed to the theoretically expected 920 meV for a QW thickness of 14.5 Å and explained this deviation with the interface roughness between InGaAs QWs and AlAsSb barriers. Interface roughness is also the reason for the wide relative responsivity linewidth of 10% at 5 K for 3392 and even 20% for 3394; comparable longer wavelength $\mathrm{In}_{0.53}\mathrm{Ga}_{0.47}\mathrm{As}$–$\mathrm{In}_{0.52}\mathrm{Al}_{048}\mathrm{As}$ QCDs have significantly narrower linewidths, such as the 4.7 μm QCD N1022 discussed previously with 3.7% at 5 K.

The weak shoulder of 3392's responsivity peaking at 670 meV with 0.25 mA/W at 5 K can be assigned to the diagonal backward $\mathrm{A}_1 \rightarrow \mathrm{H}_2$ transition followed by the $\mathrm{H}_2 \rightarrow \mathrm{A}_2$ extractor path: due to the thin barrier between QW H and A, the oscillator strength $f_{\mathrm{osc}}^{A_1,H_2} = 0.106$ is sufficiently high to lead to a measurable photocurrent.

The measured peak absorptions per double pass amount to 3% for 3392 and 1.2% for 3394, they also agree well with the values calculated using Fermi's golden rule (3) of 2.95% for 3392 and 0.84% for 3394. This weak absorption efficiency $\eta_{A_1}^{A_2,B_1}$ is caused by the low ($\mathrm{A}_1 \rightarrow \mathrm{A}_2$, $\mathrm{A}_1 \rightarrow \mathrm{B}_1$) oscillator strengths of (0.225, 0.0598) for 3392 and (0.158, 0.114) for 3394. As the oscillator strengths obey the sum rule $\sum_F f_{\mathrm{osc}}^{A_1,F} = \mathrm{const.}$ [33], a reduction of $f_{\mathrm{osc}}^{A_1,H_1} = 0.367$ and $f_{\mathrm{osc}}^{A_1,H_2} = 0.106$ would result in an increase of $\eta_{A_1}^{A_2,B_1}$

The Johnson noise-limited detectivities D^* of 3392 and 3394 were calculated with (4) using measured values for the peak responsivity R_p and R_0A. At 300 K, 3392 has an R_0A of 47.9 $\Omega \mathrm{cm}^2$ resulting in a D^* of 8.2×10^7 Jones; the corresponding values for 3394 are $R_0A = 24.5$ $\Omega \mathrm{cm}^2$ and $D^* = 1.2 \times 10^7$ Jones. D^*_{BLIP} amounts to 1.15×10^{12} Jones for 3392, respectively, 1.47×10^{11} Jones for 3394. As the R_0A measurements are limited by the maximal source meter sensitivity of 5 pA to values below $\sim 10^7$ $\Omega \mathrm{cm}^2$, the measured D^* shown in Fig. 14 are extrapolated to determine T_{BLIP}. The values obtained with this extrapolation are $T_{\mathrm{BLIP}} = 5$ K for

3392 and $T_{\mathrm{BLIP}} = 70$ K for 3394. The higher T_{BLIP} of 3394 is explained by its shorter operation wavelength, resulting in a higher R_0A and thus a higher D^*. The low T_{BLIP} s are a consequence of the weak absorption efficiencies of 3392 and 3394.

A redo of 3392, EP745, with thicker extractor barriers, especially between QW H and A', was designed to suppress the high energy shoulder of 3392; another benefit of the thicker barrier between QW H and A' is the higher oscillator strength and thus absorption efficiency between A_1 and A_2 respectively A_1 and B_1. The overall extraction efficiency does not suffer from a thicker barrier at the low-energy end of the extractor: once an extracted electron reaches the thicker barrier, its recapture probability into the active QW from where it originated is negligible. As described in [34], AlAs diffusion barriers were introduced at the QW/barrier interfaces to reduce the Sb segregation between QW and barrier. EP745 was grown at FIRST laboratory, ETH Zurich, on a Veeco GEN II MBE system.

The responsivity of EP745 is shown in Fig. 15. Compared with 3392, two main differences are observed: the linewidth of EP745 is 35% smaller and the high energy shoulder at 5400 cm^{-1} is not present in EP745's responsivity. This shows that both the AlAs interdiffusion barriers at the interfaces and the thicker barrier between QWs H and A' have the expected effects of improving the interface abruptness and lowering the $\mathrm{A}'_1 \rightarrow \mathrm{H}_2$ oscillator strength. The AlAs diffusion barriers used in EP745 lead to a significantly higher device resistance compared to 3392: at 200 K, $R_0A = 8.9 \times 10^6$ $\Omega \mathrm{cm}^2$ for EP745 compared to 4.3×10^3 $\Omega \mathrm{cm}^2$ for 3392. As a consequence of the high R_0A, the Johnson current noise is low and the Johnson noise limited detectivity D^* is high, namely 2.9×10^{10} Jones at 200 K. If D^* is extrapolated towards lower temperatures, it equals the 300 K background limited hemispherical $D^*_{\mathrm{BLIP}} = 1.15 \times 10^{12}$ Jones at $T_{\mathrm{BLIP}} = 100$ K.

At this point, a comparison with NIR detectors on the market is due: For wavelengths below 2.5 μm, commercial InGaAs interband photodetectors are available which show significantly better performance: the Judson technologies J23-xxx-2.6 with a
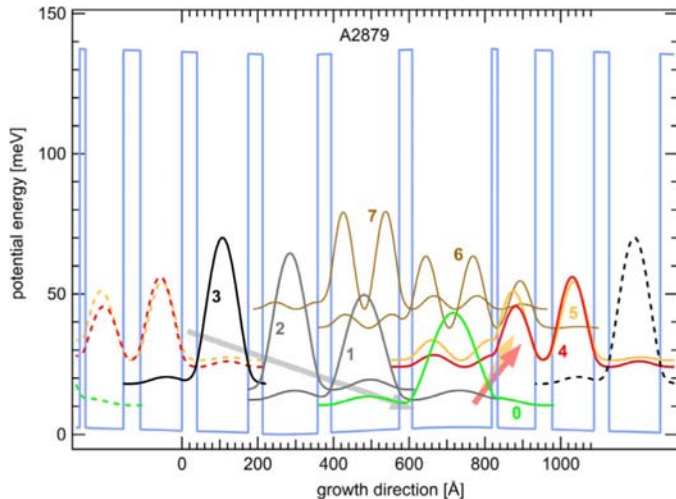
Fig. 16. Self-consistently calculated conduction band structure of the THz QWIP A2879 at 10 K. One full period, surrounded by adjacent parts of the previous and next period, is shown. The observed transitions take place between the ground state 0 and the upper states 4 and 5 and have computed energies of 13.7 and 16.0 meV. The extraction cascade consists of the states 3,2,1.

Fig. 17. Photocurrent spectra of the THz QCD. Different peaks are identifiable with calculated transition energies.

50% cutoff wavelength of $\lambda_c = 2.6\ \mu$m has a room temperature $D^* = 6 \times 10^{10}$ Jones, which increases to $D^* = 3.6 \times 10^{12}$ Jones for a Peltier-cooled device with an operating temperature of 188 K. At this temperature, InAs detectors with $\lambda_c = 3.3$ μm have similar D^*. As both InAs and InGaAs are close to the theoretical limit of D^* and have mature and cost-efficient material growth and processing, possible commercial interest to ISB photodetectors at wavelengths below 3.3 μm narrows down to applications which require fast detection speed or intrinsically narrow linewidths. One example is 3-D imaging based on the time-of-flight distance measurement principle, where the depth resolution is proportional to the light pulse frequency. In yet another line of application using mainly their small linewidth, QCD stacks detecting at slightly different wavelengths would provide a rough estimation on spectral composition without requiring a grating or interferometric spectrometer; a prospective market for such NIR spectroscopy is noninvasive determination of glucose concentration in human blood by measuring glucose absorption features around 3 μm.

C. THz QCD

The THz radiation region is loosely defined by the frequency range of 0.1 to 10 THz (30 to 3000 μm) and attracts interest from sectors as diverse as the semiconductor, medical, manufacturing, space, and defense industry [35]. For radiation sources and detectors, this region is often referred to as THz gap, as it lies between microwaves, the high frequency extreme of electronic devices, and infrared, the low frequency extreme of photonic devices. To detect THz radiation, bolometers are an established technology for certain applications. ISB THz QWIP detectors are also an emerging technology [36]. Quantum cascade lasers were demonstrated at wavelengths up to 250 μm [37], showing that quantum cascades are also well suited for THz devices. The absence of dark current in QCDs becomes even more beneficial at THz detection frequencies compared to QWIPs, as their dark current increases with decreasing detection frequency.
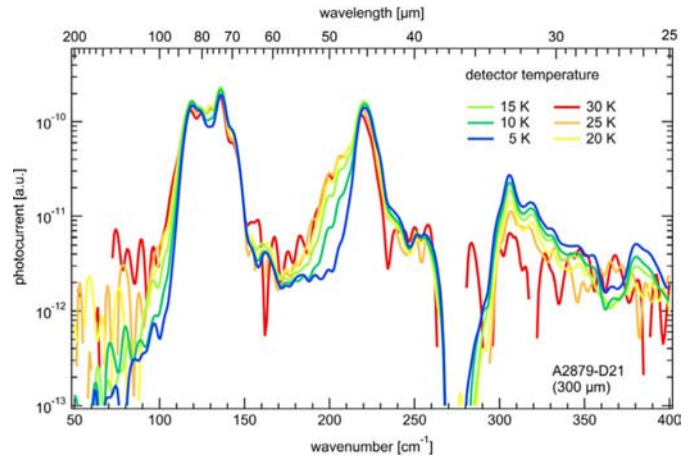
Graf *et al.* [38] published a THz QCD detecting at 84 μm (15 meV) with GaAs QWs and $Al_{0.15}Ga_{0.85}As$ barriers. Fig. 16 shows the conduction band profile computed with a self-consistent Schrödinger-Poisson solver. The active QW lies at 700 nm in the figure and is doped to 6×10^{15} cm^{-3}. Starting with the second barrier from the left, the layer thicknesses in Å are **45**, 110, **40**, 135, **38**, 145, **36**, 180, **34**, 210, **15**, 100 where bold typeface denotes barriers.

In Fig. 17, the photocurrent spectrum of the THz QCD at temperatures between 5 and 30 K is depicted. At higher temperatures, the detector signal is buried in the rising Johnson noise floor. The photocurrent peaks at 84 μm (14.8 meV) and 74 μm, (16.8 meV) which is in good agreement with the calculated ISB transition energies between level 0 and level 4 respectively 5 of 13.6 meV and 16 meV. The additional peaks at 46.3 μm and 33.7 μm are due to ISB transition into states 6 and 7. The responsivity was measured to be 8.6 mA/W at 87 μm and 10 K and the detectivity amounted to 5×10^7 Jones.

Compared with the results of a THz heterojunction photodetector based on internal photoemission [39], those results are about two orders of magnitude lower. However, the THz QCD is believed to have room for improvement [38], especially by increasing the doping density and optimizing the bandstructure for high absorption and escape probability.

D. Broadband QCD

Up to now, it was not clear whether a QCD with a spectrally broad response would—at least partially—preserve the good noise properties of the standard narrow response QCD. Recently, a MIR QCD based on lattice-matched InGaAs–InAlAs with a relative linewidth of 27% was designed and fabricated by Hofstetter *et al.* [40]. It makes use of 26 carefully designed active region stages spanning a wavelength range between 4.7 and 7.4 μm (measured at 10% of the peak responsivity). These stages were arbitrarily divided into six smaller groups having very similar extraction cascades. Within a group, only the first two active QWs were changed in order to produce slightly different absorption spectra for each stage.

As shown in Fig. 18(a), the 10 K responsivity peaks at 1950 cm^{-1} (242 meV) with 13 mA/W. The FWHM at this low

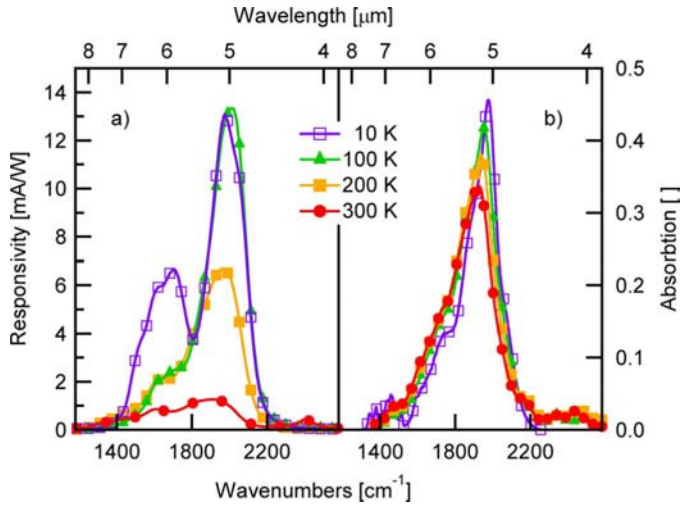Fig. 18. (a) Responsivity and (b) absorption spectra of the broadband QCD at 10 K, 100 K, 200 K, and 300 K.

Fig. 20. Normalized photocurrent of the QCDs presented in this work. They span a wavelength range from 2.05 μm (4880 cm^{-1}) to 84 μm (120 cm^{-1}).
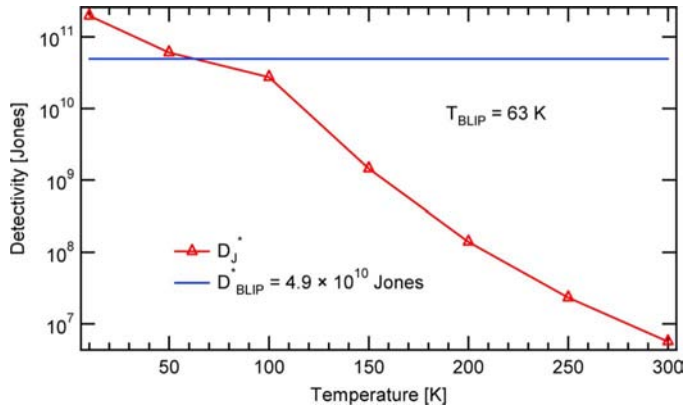

Fig. 19. Detectivity of the broadband QCD as a function of temperature along with a calculated value of the background limited detectivity.

temperature is 420 cm^{-1} (ΔE = 52 meV, ΔE/E = 21.5%). When going to 300 K, a responsivity of 1.25 mA/W peaking at 1920 cm^{-1} (E = 238 meV) was observed, with a FWHM of 525 cm^{-1} (ΔE = 65 meV, ΔE/E = 27.3%). Absorption spectra measured using a multipass waveguide configuration are shown in Fig. 18(b) for selected temperatures of 10, 100, 200, and 300 K. They agree quite well with the responsivity curves at the corresponding temperatures.

Despite the large detection spectrum, the noise properties of this device were not too adversely affected: as presented in Fig. 19, the background limited detectivity amounts to 1.55×10^{10} Jones up to a temperature T_{BLIP} of 110 K. Although not yet being fully optimized in its performance, this device is a first step towards semiconductor based ISB detectors for spectrally broad applications such as spectroscopy.

IV. CONCLUSION

QCDs are an emerging technology which is shown to encompass wavelengths from the near-infrared to the THz region as shown in Fig. 20. The design of QCDs has proven to be reliable and robust. Especially in the MIR range around 4 to 17 μm, well-established semiconductor material systems and
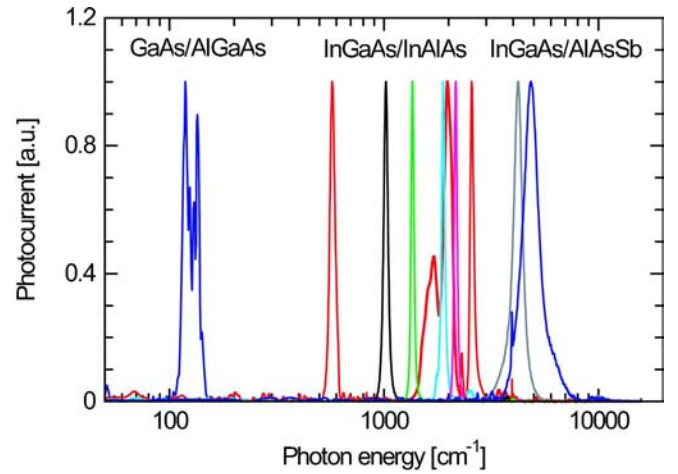
processing procedures are available. Accordingly, we demonstrated QCDs in the NIR fabricated from InGaAs–AlAsSb, in the midIR using InGaAs/InAlAs, and in the THz-region using GaAs–AlGaAs materials. A chirped QCD design is a first step towards semiconductor-based ISB detectors for spectrally broad applications. To cite just two examples of remarkably high performance, we would like to mention a QCD sensitive at 5.35 μm which was tested at frequencies up to 23 GHz; while an InGaAs–InAlAs-based, strain-compensated QCD at 3.96 μm reached a background limited detectivity in excess of 10^{11} Jones at 108 K. Together with the high speed and design flexibility, this makes QCDs very interesting candidates for applications in this wavelength range. However, the successful integration of a QCD in applications such as astronomy, 3-D imaging, or even telecommunication remains to be demonstrated. Considerable margin for improvement, especially in terms of room temperature detectivity and responsivity, has been identified. As one typical example, the device resistance can be greatly influenced by the use of thicker barrier layers, higher lying extractor states and carefully adapted doping levels.

REFERENCES

[1] B. F. Levine, K. K. Choi, C. G. Bethea, J. Walker, and R. J. Malik, "New 10 μm infrared detector using intersubband absorption in resonant tunneling GaAlAs superlattices," *Appl. Phys. Lett.*, vol. 50, no. 16, pp. 1092–1094, 1987.
[2] H. Schneider and H. C. Liu, *Quantum Well Infrared Photodetectors*. Berlin, Germany: Springer-Verlag, 2006.
[3] H. C. Liu, "Dependence of absorption-spectrum and responsivity on the upper state position in quantum-well intersubband photodetectors," *J. Appl. Phys.*, vol. 73, no. 6, p. 3062, 1993.
[4] K. M. S. V. Bandara, J. W. Choe, M. H. Francombe, A. G. U. Perera, and Y. F. Lin, "GaAs/AlGaAs superlattice miniband detector with 14.5 μm peak response," *Appl. Phys. Lett.*, vol. 60, no. 24, pp. 3022–3024, 1992.
[5] S. D. Gunapala, S. V. Bandara, J. K. Liu, C. J. Hill, S. B. Rafol, J. M. Mumolo, J. T. Trinh, M. Z. Tidrow, and P. D. LeVan, "Development of midwavelength and long-wavelength megapixel portable QWIP imaging cameras," *Infrared Phys. Technol.*, vol. 47, no. 1–2, pp. 67–75, 2005.
[6] H. Schneider, P. Koidl, F. Fuchs, B. Dischler, K. Schwarz, and J. D. Ralston, "Photovoltaic intersubband detectors for 3–5 μm using GaAs quantum-wells sandwiched between AlAs tunnel barriers," *Semicond. Sci. Technol.*, vol. 6, no. 12C, p. C120, 1991.

[7] H. Schneider, K. Kheng, M. Ramsteiner, J. D. Ralston, F. Fuchs, and P. Koidl, "Transport asymmetry and photovoltaic response in (AlGa)As/AlAs/GaAs/(AlGa)As single-barrier quantum-well infrared detectors," *Appl. Phys. Lett.*, vol. 60, no. 12, p. 1471, 1992.

[8] H. Schneider, C. Schonbein, M. Walther, K. Schwarz, J. Fleissner, and P. Koidl, "Photovoltaic quantum well infrared photodetectors: The four-zone scheme," *Appl. Phys. Lett.*, vol. 71, no. 2, pp. 246–248, 1997.

[9] H. Schneider, M. Walther, J. Fleissner, R. Rehm, E. Diwo, K. Schwarz, P. Koidl, G. Weimann, J. Ziegler, R. Breiter, and W. A. Cabanski, "Low-noise QWIPs for FPA sensors with high thermal resolution," *Infrared Technol. Applicat. XXVI*, vol. 4130, no. 1, pp. 353–362, 2000.

[10] H. Schneider, "Optimized performance of quantum well infrared detectors: Photovoltaic versus photoconductive operation," *J. Appl. Phys.*, vol. 74, no. 7, p. 4789, 1993.

[11] D. Hofstetter, M. Beck, and J. Faist, "Quantum-cascade laser structures as photodetectors," *Appl. Phys. Lett.*, vol. 81, no. 15, pp. 2683–2685, 2002.

[12] L. Gendron, M. Carras, A. Huynh, V. Ortiz, C. Koeniguer, and V. Berger, "Quantum cascade photodetector," *Appl. Phys. Lett.*, vol. 85, no. 14, pp. 2824–2826, 2004.

[13] L. Gendron, C. Koeniguer, V. Berger, and X. Marcadet, "High resistance narrow band quantum cascade photodetectors," *Appl. Phys. Lett.*, vol. 86, no. 12, p. 121116, 2005.

[14] M. Helm, *The Basic Physics of Intersubband Transitions, vol. 62 of Semiconductors and Semimetals*. London, U.K.: Academic, 2000.

[15] H. Liu, M. Buchanan, and Z. Wasilewski, "How good is the polarization selection rule for intersubband transitions?," *Appl. Phys. Lett.*, vol. 72, no. 14, pp. 1682–1684, 1998.

[16] C. Koeniguer, G. Dubois, A. Gomez, and V. Berger, "Electronic transport in quantum cascade structures at equilibrium," *Phys. Rev. B*, vol. 74, no. 23, p. 235325, 2006.

[17] M. Graf, N. Hoyler, M. Giovannini, J. Faist, and D. Hofstetter, "InP-based quantum cascade detectors in the midinfrared," *Appl. Phys. Lett.*, vol. 88, no. 24, p. 241118, 2006.

[18] D. C. Larrabee, G. A. Khodaparast, J. Kono, K. Ueda, Y. Nakajima, M. Nakai, S. Sasa, M. Inoue, K. I. Kolokolov, J. Li, and C. Z. Ning, "Temperature dependence of intersubband transitions in InAs/AlSb quantum wells," *Appl. Phys. Lett.*, vol. 83, no. 19, pp. 3936–3938, 2003.

[19] F. R. Giorgetta, E. Baumann, M. Graf, L. Ajili, N. Hoyler, M. Giovannini, J. Faist, D. Hofstetter, P. Krötz, and G. Sonnabend, "16.5 μm quantum cascade detector using miniband transport," *Appl. Phys. Lett.*, vol. 90, no. 23, p. 231111, 2007.

[20] D. Hofstetter, M. Graf, T. Aellen, J. Faist, L. Hvozdara, and S. Blaser, "23 GHz operation of a room temperature photovoltaic quantum cascade detector at 5.35 μm," *Appl. Phys. Lett.*, vol. 89, no. 6, p. 061119, 2006.

[21] H. C. Liu and J. Li, "Quantum well intersubband heterodyne infrared detection up to 82 GHz," *Appl. Phys. Lett.*, vol. 67, no. 11, pp. 1594–1596, 1995.

[22] I. Vurgaftman, J. R. Meyer, and L. R. Ram-Mohan, "Band parameters for III–V compound semiconductors and their alloys," *J. Appl. Phys.*, vol. 89, no. 11, pp. 5815–5875, 2001.

[23] D. Hofstetter, S.-S. Schad, H. Wu, W. J. Schaff, and L. F. Eastman, "GaN/AlN-based quantum-well infrared photodetector for 1.55 μm," *Appl. Phys. Lett.*, vol. 83, no. 3, pp. 572–574, 2003.

[24] F. R. Giorgetta, E. Baumann, D. Hofstetter, S. Leconte, F. Guillot, E. Bellet-Amalric, and E. Monroy, "High frequency (f = 2.37 GHz) room temperature operation of 1.55 μm AlN/GaN-based intersubband detector," *Electron. Lett.*, vol. 43, pp. 185–186, 2007.

[25] M. Rochat, D. Hofstetter, M. Beck, and J. Faist, "Long-wavelength (16 μm), room-temperature, single-frequency quantum-cascade lasers based on a bound-to-continuum transition," *Appl. Phys. Lett.*, vol. 79, no. 26, pp. 4271–4273, 2001.

[26] F. R. Giorgetta, E. Baumann, R. Theron, M. L. Pellaton, D. Hofstetter, M. Fischer, and J. Faist, "Short wavelength (4 μm) quantum cascade detector based on strain compensated InGaAs/InAlAs," *Appl. Phys. Lett.*, vol. 92, no. 12, p. 121101, 2008.

[27] F. Capasso, K. Mohammed, and A. Y. Cho, "Resonant tunneling through double barriers, perpendicular quantum transport phenomena in superlattices, and their device applications," *IEEE J. Quantum Electron.*, vol. QE-22, no. 9, pp. 1853–1869, Sep. 1986.

[28] P. Cristea, Y. Fedoryshyn, J. F. Holzman, F. Robin, H. Jäckel, E. Müller, and J. Faist, "Tuning the intersubband absorption in strained AlAsSb/InGaAs quantum wells towards the telecommunications wavelength range," *J. Appl. Phys.*, vol. 100, no. 11, p. 116104, 2006.

[29] Q. K. Yang, C. Manz, W. Bronner, K. Kohler, and J. Wagner, "Room-temperature short-wavelength (lambda similar to 3.7–3.9 mu m) GaInAs/AlAsSb quantum-cascade lasers," *Appl. Phys. Lett.*, vol. 88, no. 12, p. 121127, 2006.

[30] C. V.-B. Tribuzy, S. Ohser, M. Priegnitz, S. Winnerl, H. Schneider, M. Helm, J. Neuhaus, T. Dekorsy, K. Biermann, and H. Künzel, "Inefficiency of intervalley transfer in narrow InGaAs/AlAsSb quantum wells," *Phys. Stat. Sol. (c)*, vol. 5, no. 1, pp. 229–231, 2008.

[31] F. R. Giorgetta, E. Baumann, D. Hofstetter, C. Manz, Q. Yang, K. Köhler, and M. Graf, "InGaAs/AlAsSb quantum cascade detectors operating in the near infrared," *Appl. Phys. Lett.*, vol. 91, p. 111115, 2007.

[32] A. Neogi, H. Yoshida, T. Mozume, N. Georgiev, T. Akiyama, and O. Wada, "Absorption saturation of near-infrared intersubband transition in lattice-matched InGaAs/AlAsSb quantum wells," *Physica E*, vol. 7, no. 1–2, pp. 183–186, 2000.

[33] C. Sirtori, F. Capasso, J. Faist, and S. Scandolo, "Nonparabolicity and a sum-rule associated with bound-to-bound and bound-to-continuum intersubband transitions in quantum-wells," *Phys. Rev. B*, vol. 50, no. 12, p. 8663, 1994.

[34] P. Cristea, Y. Fedoryshyn, and H. Jäckel, "Growth of AlAsSb/InGaAs mbe-layers for all-optical switches," *J. Cryst. Growth*, vol. 278, no. 1–4, pp. 544–547, 2005.

[35] B. Ferguson and X. C. Zhang, "Materials for terahertz science and technology," *Nat. Mater.*, vol. 1, no. 1, pp. 26–33, 2002.

[36] H. Liu, H. Luo, C. Ying Song, Z. Wasilewski, A. SpringThorpe, and J. Cao, "Terahertz quantum well photodetectors," *IEEE J. Sel. Topics Quantum Electron.*, vol. 14, no. 2, pp. 374–377, Mar.–Apr. 2008.

[37] C. Walther, M. Fischer, G. Scalari, R. Terazzi, N. Hoyler, and J. Faist, "Quantum cascade lasers operating from 1.2 to 1.6 THz," *Appl. Phys. Lett.*, vol. 91, no. 13, p. 131122, 2007.

[38] M. Graf, G. Scalari, D. Hofstetter, J. Faist, H. Beere, E. Linfield, D. Ritchie, and G. Davies, "Terahertz range quantum well infrared photodetector," *Appl. Phys. Lett.*, vol. 84, no. 4, pp. 475–477, 2004.

[39] S. G. Matsik, M. B. M. Rinzan, A. G. U. Perera, H. C. Liu, Z. R. Wasilewski, and M. Buchanan, "Cutoff tailorability of heterojunction terahertz detectors," *Appl. Phys. Lett.*, vol. 82, no. 1, pp. 139–141, 2003.

[40] D. Hofstetter, F. R. Giorgetta, E. Baumann, Q. Yang, C. Manz, and K. Köhler, "Mid-infrared quantum cascade detector with a spectrally broad response," *Appl. Phys. Lett.*, vol. 93, no. 22, p. 221106, Sep. 2008.

Fabrizio R. Giorgetta received he M.Sc. degree in electrical engineering from the Swiss Federal Institute of Technology (ETHZ), Zurich, Switzerland, in 2003 and the Ph.D. degree in physics from the University of Neuchatel, Neuchatel, Switzerland, in 2007 for his work on quantum cascade detectors.

Since 2008, he has been working on fiber laser frequency combs as a Guest Researcher with the National Institute of Standards and Technology, Boulder, CO.

Esther Baumann received the M.Sc. degree in electrical engineering from the Swiss Federal Institute of Technology (ETHZ), Zurich, Switzerland, in 2003 and the Ph.D. degree in physics from the University of Neuchatel, Neuchatel, Switzerland, in 2007 for her work on photovoltaic light detection in III-Nitrides intersubband systems.

Since 2008, she has been working on fiber laser frequency combs as a Guest Researcher with the National Institute of Standards and Technology, Boulder, CO.

Marcel Graf was born in Switzerland in 1973. He received the dipl. phys. degree in experimental physics from the Swiss Federal Institute of Technology (ETH), Zürich, Switzerland, in 1998 and the Ph.D. degree from the Physics Institute, University of Neuchâtel, Neuchâtel, Switzerland, in 2006 for his work ong quantum cascade detectors in the far- and mid-infrared wavelength range.

He was a Visiting Scientist with the Institute of Microstructural Sciences, National Research Council of Canada, Ottawa, ON, Canada, on a postdoctoral fellowship of the Swiss National Science Foundation in 2006–2007. Currently, he is with the Department of Electrical and Computer Engineering, University of Waterloo, Waterloo, ON, Canada and with the Institute of Microstructural Sciences, National Research Council of Canada, Ottawa. His research interests cover semiconductor physics and technology, optoelectronics, terahertz radiation detection and generation, and numerical simulation.

Quankui Yang received the B.Sc. degree in physics from Wuhan University, Wuhan, China, in 1995 and the Ph.D. degree in solid-state electronics from the Chinese Academy of Sciences, Shanghai, in 2000.

He joined the Fraunhofer-Institut für Angewandte Festkörperphysik (IAF), Freiburg, Germany, as a Postdoctoral Research Fellow in 2000 and became a permanent Research Scientist in 2002. His work mainly focuses on the development and application of quantum cascade lasers. He has coauthored more than 40 peer-reviewed journal papers.

Christian Manz received the Dipl.-Ing. degree in physical engineering from Heilbronn University, Heilbronn, Germany, in 1996.

He joined the Fraunhofer-Institut für Angewandte Festkörperphysik (IAF), Freiburg, Germany, in 1997. His work mainly focuses on the epitaxial growth of III–V semiconductor structures, in particular (AlGaIn)(AsSb) laser and detector structures.

Klaus Köhler was born in 1951. He received the Diploma and Ph.D. degree in physics from the Technical University of Karlsruhe, Karlsruhe, Germany, in 1978 and 1981, respectively.

From 1981 to 1982, he was with the IBM Research Laboratory, San Jose, CA, investigating electrical discharges for dry-etch processes. From 1983 to 1986, he was with the Max-Planck-Institut für Festkörperforschung, Stuttgart, Germany, where he conducted optical investigations on III–V semiconductor heterostructures. Since 1987, he has been with the Fraunhofer-Institut für Angewandte Festkörperphysik (IAF), Freiburg, Germany, working on the molecular beam epitaxy as well as on the metal–organic vapor phase epitaxy of III–V semiconductor heterostructures.

Dr. Köhler is a member of the German Physical Society (DPG)

Harvey E. Beere was born in Cambridge, U.K., in 1970. He received the M.Eng. degree in electrical and electronic engineering from Imperial College, London, U.K., in 1993 and the Ph.D. degree in physics from the University of Cambridge, Cambridge, in 1999. His studies focused on the selective area growth of III–V semiconductor compounds by using a focused ion beam source with molecular beam epitaxial (MBE) growth.

He has been a Postdoctoral Research Associate with the Semiconductor Physics Group, University of Cambridge, since 1999, where his work has concentrated on the growth and development of novel electrical and optical semiconductor devices, including quantum-cascade lasers. He has over ten years of experience in MBE growth and has coauthored over 20 papers.

David Ritchie received the degree in physics from the University of Oxford, Oxford, U.K., in 1980 and the D.Phil. degree from the University of Sussex, Sussex, U.K., in 1986 studying the physics of mixtures of liquid 3He and 4He at milli-kelvin temperatures.

He is a Professor of Experimental Physics at the University of Cambridge, Cambridge, U.K., and Head of the Semiconductor Physics group. He has been working on III-V semiconductor physics and has extensive experience of the growth, fabrication, and measurement of low dimensional electronic and optical structures. He has been coauthor of over 850 paper.

Dr. Ritchie was the recipient of the 2008 Tabor Medal and Prize by the U.K. Institute of Physics for distinguished research in surface or nanoscale physics.

Edmund Linfield received the B.A. (Hons.) degree in physics and the M.A. degree from the University of Cambridge, Cambridge, U.K., in 1986 and 1991, respectively, and the Ph.D. degree in semiconductor physics from the Cavendish Laboratory, University of Cambridge, in 1991.

He continued his research as a Post-Doctoral Researcher Associate with the Cavendish Laboratory, University of Cambridge, until 1997, when he was appointed as an Assistant Director of Research. He also became a Fellow of Gonville and Caius College, Cambridge. In 2004, he moved to the University of Leeds, Leeds, U.K., to take up the Chair of Terahertz Electronics, where he is currently also Director of the Institute of Microwaves and Photonics. His research interests include semiconductor growth and device fabrication, terahertz-frequency optics and electronics, and nanotechnology.

Alexander G. Davies received the first class B.Sc. (Hons.) degree in chemical physics from the University of Bristol, Bristol, U.K., in 1987 and the Ph.D. degree in semiconductor physics from the Cavendish Laboratory, University of Cambridge, Cambridge, U.K., in 1991.

After spending three years as an Australian Research Council Postdoctoral Research Fellow with the University of New South Wales, Sydney, Australia, he returned to the University of Cambridge in 1995 as a Royal Society University Research Fellow. In 2002 he moved to the University of Leeds, Leeds, U.K., to take up the Chair of Electronic and Photonic Engineering, where he is currently also Director of Research and Deputy Head of the School of Electronic and Electrical Engineering. He is Associate Editor of the *Philosophical Transactions of the Royal Society*. His research interests include semiconductor nanostructures, terahertz-frequency optics and electronics, and bionanotechnology.

Yuriy Fedoryshyn received the B.S. and M.S. degrees from Lviv Polytechnic National University, Ukraine, in 2001 and 2002, respectively.

In 2002, he joined the Group of Mesoscopic Physics, University of Neuchatel, Neuchatel, Switzerland, where he has been engaged in research on quantum cascade lasers based on waveguide design with a Ge layer. In 2004, he joined the Communication Photonics Group, ETH Zurich, Zurich, Switzerland, where his current research is focused on development of an ultra-fast all-optical switch based on intersubband transitions in InGaAs–AlAsSb quantum wells.

Heinz Jäckel (M'87) received the Ph.D. degree in electrical engineering from the Swiss Federal Institute of Technology (ETH), Zurich, in 1979. His dissertation focused on photon statistics and the dynamic behavior of semiconductor lasers.

In 1980, he joined IBM, where he held scientific and management positions for 13 years in the research laboratories of IBM in Rüschlikon, Switzerland, and Yorktown Heights, NY. During this time, he carried out research projects in the field of device and circuit design for superconducting Josephson Junction Computers, GaAs-Mesfet logic, and memory integrated circuits (ICs). In the field of optoelectronics, he worked on short-wave and 980-nm power semiconductor lasers and ultrafast diode lasers and photodetectors. Since 1993, he has been Full Professor of Analog Electronics with ETH. The research activities of his High Speed Electronics and Photonics-group concentrate on ultrafast transistors (mainly InP-based heterojunction bipolartransistors), circuits for multi-10-Gb electronics, IC design, and RF circuits for mobile communication. In the area of lightwave communication, the group pursues research on photonic devices and integrated optical circuits for all-optical signal processing at terabit per second data rates.

Milan Fischer received the M.gr. degree in physics from the Charles University, Prague, Czech Republic, in 2004. He is currently working toward the Ph.D. degree at the Swiss Federal Institute of Technology (ETH), Zurich, concentrating on the growth and development of Terahertz Quantum Cascade lasers.

Jérôme Faist (M'94) was born in Switzerland. He received the Ph.D. degree in physics from the Swiss Federal Institute of Technology (ETH), Lausanne, in 1989.

From 1989 to 1991, he was with IBM Rueschlikon, Rueschlikon, Switzerland. From 1991 to 1997, he was with Bell Laboratories, Murray Hill, NJ, where he was engaged in the invention of the QC laser, demonstration of continuous-wave operation, room-temperature operation, the development of microdisk QC lasers, and distributed feedback QC lasers. He was a Full Professor with the Institute of Physics, University of Neuchâtel, Neuchâtel, Switzerland, from 1997 to June 2007. Since July 2007, he has been a Full Professor with the Institute for Quantum Electronics, ETH, Zurich, Switzerland.

Daniel Hofstetter was born in Zug, Switzerland, in 1966. From 1988 to 1993, he studied physics at the Swiss Federal Institute of Technology (ETHZ), Zurich, Switzerland. In his diploma thesis under the supervision of Prof. Dr. F.K. Kneubuehl, he carried out photoacoustic spectroscopy on fatty acids using gas lasers. He received the Ph.D. degree from the Paul Scherrer Institute, Zurich, Switzerland, in 1996, for work which included the design, fabrication, and testing of a semiconductor-based monolithically integrated Michelson interferometer for optical displacement measurement.

After an apprenticeship as an Electrical Mechanic at Landis & Gyr, Zug, Switzerland, from 1982 to 1986, he became a Physics Technician until 1988. Later, he was with the XEROX Palo Alto Research Center, Palo Alto, CA, developing single-mode InGaN-based violet semiconductor lasers (1996–1998). From 1998 to 2001, he was with the Mesoscopic Physics Group of Prof. Dr. Jerome Faist at the University of Neuchatel, Neuchatel, Switzerland, where his work concentrated on the fabrication and testing of single-mode distributed-feedback quantum-cascade (QC) lasers and high performance QC lasers. Since 2002, he has been an Assistant Professor with the University of Neuchatel. His main activities included the development of novel types of semiconductor-based devices, such as QC detectors, for the midinfrared wavelength region.